Opto-Electronic Advances

Supplementary information

2019, Vol. 2, No. 9

DOI: 10.29026/oea.2019.190019

Multifunctional inverse sensing by spatial distribution characterization of scattering photons

Lianwei Chen[1†], Yumeng Yin[2†], Yang Li[1] and Minghui Hong[1*]

[1]Department of Electrical and Computer Engineering, National University of Singapore, 4 Engineering Drive 3, 117576, Singapore; [2]Department of Computer Science, School of Computing, National University of Singapore, 117576, Singapore.

* Correspondence: M H Hong, E-mail: elehmh@nus.edu.sg

This file includes:

Supplementary information for this paper is available at https://doi.org/10.29026/oea.2019.190019

Section 1: Experimental conditions for the light direction analysis

Schematics of the experimental setup and the corresponding DL results are presented in Fig. S1. To build the training databases for the analyses of incident direction, two setups are designed to test the accuracy of the polar angle (θ) and azimuthal angle (φ), respectively (0–180 degree for azimuthal angle φ horizontally and 45–90 degree for θ polar angle vertically). For the polar angle detection, the laser source is placed 30 cm away from the irradiation point. The distance between the laser source and the irradiation point is kept constant. The polar angle of the laser source decreases from 90 to 45 degrees gradually. The CMOS is used to capture the scattered photon profile. The details of the camera parameters can be found in **Section 2**. It should be noted that the laser source is out of the field-of-view of the CMOS image. A similar setup is designed for the detection of the azimuthal angle. In this setup, the laser source is kept 30 cm away from the irradiation point and 5 cm from the horizontal surface. The laser source rotates along the horizontal direction from 0 to 180 degrees. The same CMOS is used to record this process. The results after CNN DL are presented in Fig. S1(c). As can be seen in the figure, the accuracies for the analyses can reach 100%. Furthermore, with the same setup, we have tested that our method can accurately detect the small incident angle variation (From -2 to 2 degrees with 1-degree increment). The accuracy of the CNN DL method is presented in Fig. 1(d).

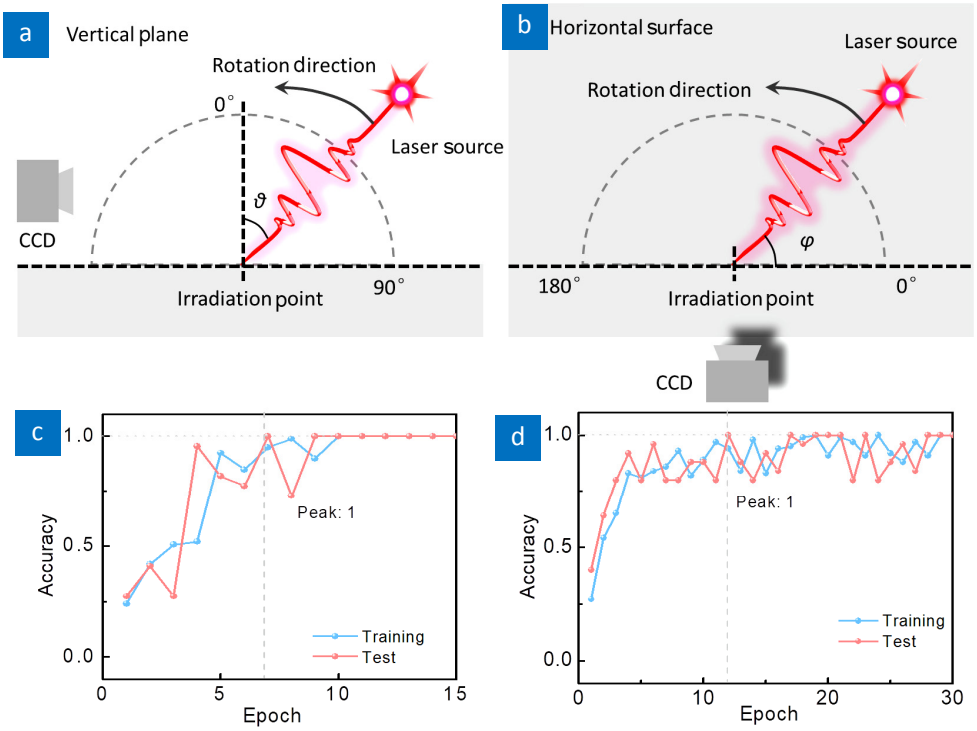

Fig. S1 | Schematic diagram of the imaging capture experimental setup for rotation in (**a**) vertical plane and (**b**) horizontal plane. The dash lines are references for demonstration purpose and they do not exist in the experiment. (**c**) Results for the DL to detect the rotation along both the horizontal direction and vertical direction. The results of the accuracy testing are presented in (**d**).

In Fig. S1(c), the accuracy of the function increases to 100% in less than 10 epochs. It should be noted that the DL model chosen is widely used for the applications of the identification of the certain patterns in imaging. For this experiment, it is a typical problem for this DL model. In the experiment, the increment is 9 degrees to polar and azimuthal angles. When the incident angle changes, it does not take much training time for the DL model to identify the change of the rotation in the scattered photon profile. However, for the case of the accuracy detection, it takes much more training to reach the peak value. A small variation of 1 degree is more challenging for the deep model to find the proper set of parameters.

Section 2: Summary of the camera specifications for the optical imaging

The Leica camera on the Huawei Mate 9 (MHA-AL00) is used to capture the optical images in all the experiment. The methods for each experiment are listed below:

Table S1 | Experimental conditions for data collections

Experiment number	Laser wavelength (nm)	Light condition	ISO	Shutter time (s)	Focus setting
1	606	Dark	3200	1/2	Infinite distance
2	532	Dark	3200	1/10	Infinite distance
3	532	Dark	3200	1/100	Infinite distance
4	532	Dark	3200	1/15	Infinite distance
5	532	Dark	3200	1/15	Infinite distance
6	532	Room Light	3200	1/320	Infinite distance
7	532	Room Light	3200	1/100	Infinite distance
8	532 (pump)	Under microscope	N.A.*	N.A.*	On the object
9	808	Dark	3200	1/15	On the object

*Taken with a Nikon DS-Qi2 CMOS camera.

Experiment & Corresponding Fig.	Assigned experiment number
Direction analysis in Figs. 1(d) & S1	1
Laser intensity analysis in Fig. 1(e)	2
Out-of-sight intensity analysis in Figs. 3(a) & 3(b)	3
Multi-beam monitoring in Figs. 3(c) & 3(d)	4
5-meter measurement in Fig. 3(e)	5
Noise test in Fig. 3(f)	6
Hidden objects characterization in Figs. 4(a) – 4(c)	7
Bio-dyes fluorescence analysis in Figs. 4(d) & 4(e)	8
Femtosecond laser monitoring in Figs. 4(f) – 4(h)	9

The aim of taking the images is to capture the change of the scattered photon distribution according to the variation of the physical parameters. It is found in our DL that images with a larger difference require less processing epoch and time to reach high accuracy. For every data point, 20–35 pictures are taken to build the training databases.

Section 3: Experimental conditions for bio-dyes fluorescence characterization

Rhodamine B is chosen in our experiments, which is a widely used bio-dye in fluorescence microscopy. Absorption and emission spectra of Rhodamine B are presented in the previous literature[1,2]. In our experiment, we choose a 532 nm CW laser as the pumping source because the absorption is relatively high at this wavelength.

To prepare the samples, we first dissolve Rhodamine B in water to get the solution at a concentration of 1 mM. Glass substrate is cleaned with DI water and the upper surface is rinsed with the Rhodamine solution for three times. One blower is then used to provide hot air to dry the substrate. Femtosecond laser (Coherent, 1000 Hz repetition rate, 100 fs pulse duration, 800 nm wavelength) is used. The average energy of the laser output is controlled to be 0.09 W. A scanner (IntelliSCAN 14) is used to focus the laser beam and scan on the sample surface. The scanning speed is 100 mm/s. The energy of the laser is controlled carefully so that the glass surface is not damaged. However, the laser is sufficient to remove Rhodamine B molecules. Patterns of square shape are created. The dimension of the pattern is set to be 70 μm× 35 μm. After the laser fabrication, the sample is sent for characterization without washing.

An optical microscope is used for the characterization. The setup for the characterization is compatible with other microscope systems. In this setup, we combine a pumping source to provide the excitation for the fluorescence emission. To filter out the pumping light from the CMOS, one long-pass filter is selected and it is placed between the sample and the detector. It should be noted that all these modifications are based on the commonly used components for the fluorescence microscopy. To apply our detection scheme does not require extra components. The only upgrade required is to install our inverse sensing software toolkit.

As presented in the previous literature[1,2], the parameters of the components are selected to ensure the detector mainly captures the fluorescence emission. A 532 nm CW laser (Coherent MBD-266) is chosen as the pumping source for the fluorescence emission. The light path is carefully aligned to avoid the blockage by the mechanical parts of the microscope. As the emission of the Rhodamine B centered at ~565 nm wavelength, a 550 long path filter is inserted into the optical path of the microscope to filter out the pumping light. One *XY* stage is used to provide the accurate control. One mono-color CMOS (Nikon DS-Qi2) is used to capture the picture.

For the sample, the absorption of the Rhodamine B coated sample is measured to be 0.12% when it is irradiated by 532 nm laser (Rhodamine B has the quantum yield of 0.7). In the characterization, the pumping light increases from 0 to 50 mW. The emission light intensities from the entire sample at different pumping energy are also measured. In our experiments, the Rhodamine B spreads uniformly on the substrate. The emission intensity of the pattern can be estimated by the following equation:

$$\text{Emission intensity of the pattern} = \frac{\text{Area of the pattern}}{\text{Total area}} \times \text{Total emission intesity} \quad . \tag{S1}$$

For our experiment, the spot area of the pumping laser is ~5.65×10^{-5} m^2. The Rhodamine B spreads out across the entire sample surface, which is much bigger than the spot area. The spot area is taken as the total area in equation S1. The area of the pattern is calculated to be 2.45×10^{-9} m^2. With the above information, the emission intensity of the pattern can be estimated. In our experimental conditions, the lowest emission intensity of the pattern is calculated to be 0.42 nW. It should also be noted that the glass substrate does not show any fluorescence emission under our pumping light condition.

The training data is collected by taking the optical image of the Rhodamine B islands at different pumping intensities. It should be noted that the CMOS camera provides a high-resolution image (4908×3264). To demonstrate that our concept does not require huge computational powers, we ran our experiment on a laptop (specifications of the laptop are given in **Section 5**). This image has too many pixels to be processed by the laptop. We then cut the image into sub-images with 200 pixels×90 pixels. 45 sub-images compose one training data set. The accuracy of the function after every training epoch is presented in Fig. S2.

In Fig. S2, the peak value is 0.9, which is ~10% lower than the cases presented in the manuscript. Referring to the optical image of the Rhodamine B sample (Figs. 3(a, c–e), it can be concluded that the Rhodamine B molecules aggregate on the glass surface (indicated by the shining points in the pictures). The aggregation is a random process and adds complexity to the system. Considering the small number of sub-images in every training dataset and compared to other machine learning examples 3, this accuracy is already high enough for the scattering light analysis. In machine learning, it should be noted that there is a balance between the number of the images in the training set and the accuracy of the final function. An increased number of the training data generally leads to higher accuracy. However, it also requires more computational resources to process the training data.

For the optical sensing (Fig. S3), a selected area of the same pixel number (200×90) is processed by the DL. The light intensity is given for the selected area. This detection mechanism can be directly applied to the Rhodamine B samples with the same preparation conditions. It can also be used to detect the Rhodamine B samples at different concentrations as the emission light intensity is different in the same pumping light condition.

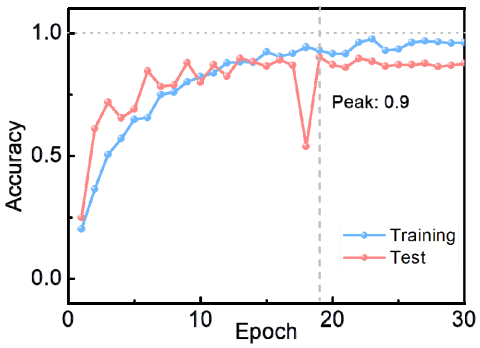

Fig. S2 | Accuracy respect to every training epoch for the Rhodamine B bio-dyes fluorescence.

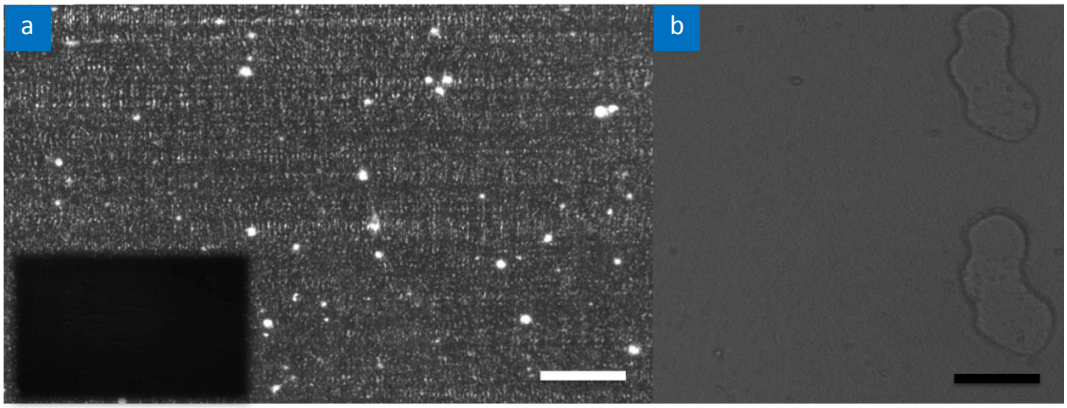

Fig. S3 | (**a**) Optical image of the Rhodamine B sample irradiated by the 532 nm pumping light (inset is the optical image of the same sample without pumping light irradiation, scale bar: 100 μm). (**b**) Sample after the laser patterning (the marks on the right are the reference area that is removed by the laser at the high output power. Except for this area, the rest are irradiated at the average laser power of 0.09 W. Compared these two areas, it can be concluded that laser with an average power of 0.09 W does not ablate the glass surface. Scale bar: 100 μm).

References in Section 3:

1. Eastman Laboratory Chemicals Catalog. *Fisher Scientific* **55** (1993-94)
2. Dixon J M, Taniguchi M, Lindsey J S. PhotochemCAD 2. A Refined Program with Accompanying Spectral Databases for Photochemical Calculations. *Photochem Photobiol* **81**, 212–213. (2005)
3. Hezaveh Y D, Levasseur L P, Marshall P J. Fast automated analysis of strong gravitational lenses with convolutional neural networks. *Nature* **548,** 555–557 (2017).

Section 4: Experimental conditions for real-time femtosecond laser intensity monitoring.

The femtosecond laser used for this experiment is the same as described in the previous section (Coherent Laser, 1000 Hz repetition rate, 100 fs pulse duration, 800 nm wavelength). The laser beam is guided into the same scanner for the laser processing. The camera is fixed to take the view of the processing stage and the scattered photon on the surrounding objects. In the fabrication experiments, the maximum average power is 3.6 W. An optical filter with 0.2 transmittance is added to control the output energy. The peak power at the focal spot goes up to GW level (Peak power = Average power/ (Repetition rate × Pulse duration)). Such high peak power is sufficient to ablate the stainless steel samples as demonstrated in Fig. S4 (also selected as the background picture in Figs. 4(d) & 4(e)). This optical image is taken with the Leica camera, the ISO (International Organization of Standardization) sensitivity is 100 and the exposure time is 10 seconds. For the calibration, the detector is placed out of the focus point with optical filters to avoid damage of the laser power meter. To measure the power of the laser beam, the power meter needs to intercept the laser beam and the laser processing is affected. For this reason, to monitor the power directly at the focal point can be hardly achieved with the conventional methods.

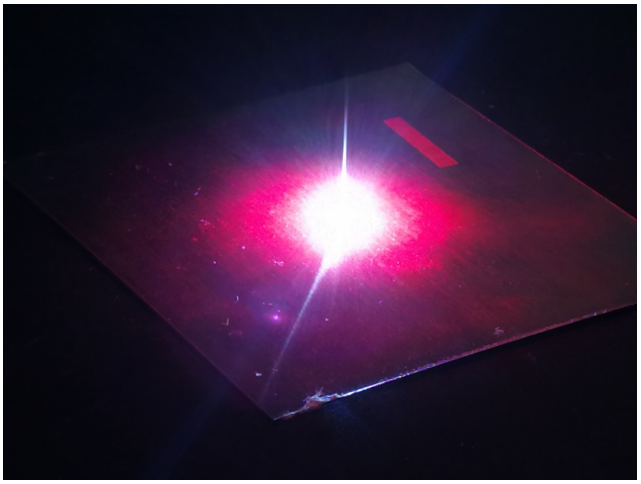

Fig. S4 | Optical image of the stainless steel during the laser ablation (the pink color mark on the top right corner is the texture fabricated by the laser)

For the dynamic laser intensity real-time monitoring as presented in Fig. 4(e), the laser ablation process is applied to make surface textures on the stainless steel. The average laser power increases step by step. The optical image is taken every 1 second through the entire process. The field of view is chosen to put the sample stage near the center of the picture in order to capture the profile of the scattered photon. The pictures are processed by the CNN DL program and the corresponding laser power is given and summarized in Fig. 4(e).

Section 5: Accuracy of the deep learning (DL) analysis for hidden objects

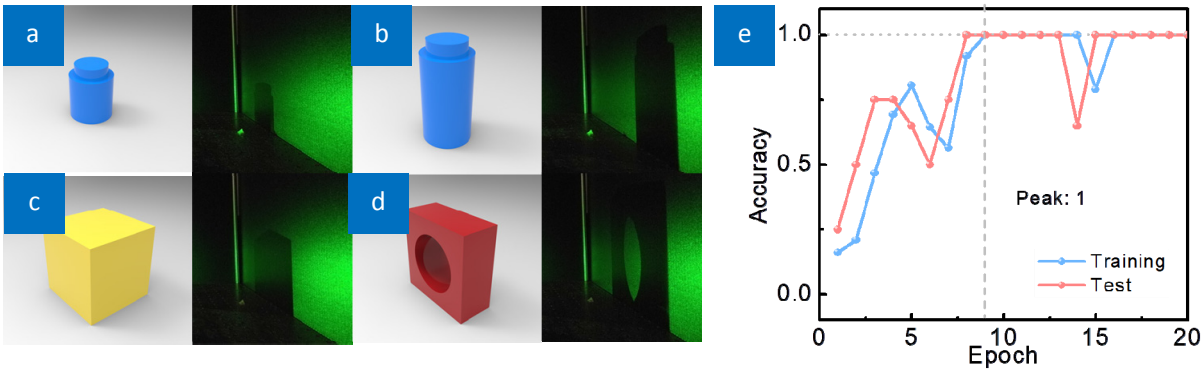

Fig. S5 | Illustration and the scattered photon profile of the 4 objects for the DL analyses: (**a**) short rod; (**b**) long rod; (**c**) cube; and (**d**) cubic donut. The accuracy respected to every training epoch is presented in (**e**). The peak value is 100% accuracy.

We select 4 objects with different features in our experiment (Fig. S5): (a) & (b) objects of similar shape but different sizes; (a) & (c) objects of similar size but different shapes; (c) & (d) objects that are solid or hollow. After the DL, our method can distinguish four objects. The accuracy goes up to 100% in our experimental conditions. It should be noted that the DL approach has been applied to a broach range of the pattern identification. This study shows a potential detection scheme with the scattered photon profile in optical engineering.

Section 6: Details of inverse sensing by CNN DL

In this section, we shall discuss the optimized approach to process the scattered photon profile with the CNN DL. The source and the complicated nature of the scattered photon profile are discussed. The complicated scattering light profile also contains abundant information for inverse optical sensing. To obtain the useful information, we develop the proper pre-processing steps specifically optimized for the scattering light analysis.

Firstly, we consider the unique properties of the scattered photon. The most important feature for the scattered photon profile is its variation under the environment illumination as demonstrated in Figs. 1(a) & 1(b). To select such key information and avoid other environmental noise, one effective approach is to rescale the image to combine the pixels. On the other hand, we consider the tasks to process the optical image and evaluate the light property of interests from the scattered photon profile. Directly working with the camera image (2976 pixels×3968 pixels) can be demanding in terms of the memory and computation requirements. The camera images taken are first converted into the images with 150×150 pixels and 150×150×3 RGB values. Firstly, to rescale the picture, we use the "resize" function from the python library cv2. We choose its interpolation method INTER_LINEAR in the library. For all the images taken by the camera, this pre-processing method is conducted in our experiment. Demonstrated by the high accuracy and relative low resources required for training process, such pre-processing proves to be extremely useful for the scattered light profile analyses.

The image after pre-processing is then analyzed by our CNN DL model. The Alexnet CNN model is applied in our case. In the experiments, the multi-class classification is required. Thus, we use the softmax activation for the multiclass classification as presented in the manuscript. Then, rectified linear units (ReLUs) activation method is used for the hidden layers in this neural network, which introduces the nonlinearity to the neural network. ReLUs functions provide the fast training speed in our case. The exact architecture of our neural network is described as follows. We control carefully the size of our neural network to make sure it can be widely used by the ordinary computational devices. The input to the neural network consists of a 150×150×3 image produced by the pre-processing method. The first hidden layer convolves 50 filters with kernel size (3, 3) followed by a rectifier nonlinearity. The padding method used for this layer is the 'same' padding. The second hidden layer convolves 50 filters with kernel size (3, 3) with the 'same' padding method. The next layer is a maxpooling layer with a pool size set as (2, 2) followed by dropout layer with a dropout set as 0.2. The final hidden layer is fully-connected and consists of 512 units. The output layer is a fully-connected layer and the number of units is set as the number of classes for each data set. The softmax activation function is used to get output with a categorical distribution.

For the settings of the neural network, we use the RMS optimizator with the learning rate and decay set as 10^{-4} and 10^{-6}, respectively. The values of all the hyperparameters and optimization parameters were selected by applying the most widely used values set in the literature. Though it is useful and promising to further study the effect of the hyperparameters and optimization parameters in a systematic manner, it is beyond the scope of the current work as such study belongs to the computational exploration for incremental development. The hyperparameters and optimization parameters are kept constant in our experiment. The values and descriptions of all hyperparameters are provided in Table S2.

Table S2 | Table for the hyperparameters.

Hyperparameter	Value (a.u.)	Descriptions
Epoches	30	Total epochs of the training process. One epoch is one set of forward pass and one backward pass of all the training examples
Minibatch	32	Number of training sets over which each update of parameters the optimizer is used.
Learning rate	5×10^{-4} (10^{-4} for Experiment 2)	Learning rate used by RMSProp activation function.
Decay	10-6	Decay for RMSProp activation function.
Dropout rate	0.2	Dropout rate used after the fully connected layer and the max pooling layer.
Pooling size	(2,2)	Pooling size for maximum pooling layer.

The evaluation procedure is also described hereby. Prior to the training procedure, 1/5 of the pictures are randomly chosen to be testing data sets and 4/5 of the pictures are used as training data sets. Testing sets are not used in the entire training process so these two sets are independent from each other, which means they are unknown to the model after the entire training process. The light property given by the DL model is then compared with the exact value from the calibration. The accuracy is calculated by the ratio of the correct predictions in the evaluation process.

To conclude, we develop a CNN DL based toolkit to analyze the scattered light profile. The pre-treatment setup is used

to reduce the abundant information in the scattered light profile as well as the resources required for the calculation. Then, a CNN DL network is constructed to process the image after the pre-processing. This processing method is different from the conventional computational approaches for optical analysis such as Finite-Difference Time-Domain method (FDTD) and Computer Simulation Technology (CST). The conventional approaches cannot be used for the inverse sensing. Our successful toolkit is fully automatic and is very effective in a controlled environment. With sufficient training, this toolkit is universal for most situations. It does not require a human engineer to tailor the code for different situations. For most of the optical setups, the design is fixed and the environment is pre-determined, which makes it possible to widely apply such inverse sensing scheme.